JACS JOURNAL OF THE AMERICAN CHEMICAL SOCIETY
Article
pubs.acs.org/JACS

Single Sublattice Endotaxial Phase Separation Driven by Charge Frustration in a Complex Oxide

Antoine Demont,[†,⊥] Ruth Sayers,[†,⊥] Maria A. Tsiamtsouri,[†,⊥] Simon Romani,[‡] Philip A. Chater,[†] Hongjun Niu,[†] Carlos Martí-Gastaldo,[†] Zhongling Xu,[†] Zengqiang Deng,[†] Yohann Bréard,[§] Michael F. Thomas,[∥] John B. Claridge,[*,†] and Matthew J. Rosseinsky[*,†]

[†]Department of Chemistry, University of Liverpool, Liverpool L69 7ZD, United Kingdom
[‡]Department of Engineering, University of Liverpool, Liverpool L69 3GH, United Kingdom
[§]Laboratoire CRISMAT, 6 Boulevard Maréchal Juin, 14050 Caen Cedex 4, France
[∥]Department of Physics, University of Liverpool, Liverpool L69 7ZE, United Kingdom

S *Supporting Information*

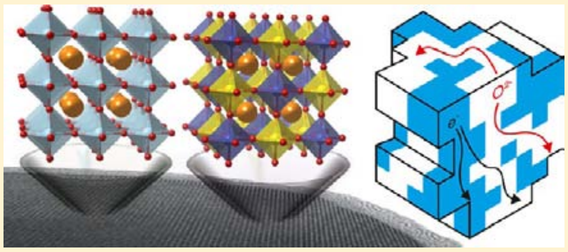

ABSTRACT: Complex transition-metal oxides are important functional materials in areas such as energy and information storage. The cubic ABO_3 perovskite is an archetypal example of this class, formed by the occupation of small octahedral B-sites within an AO_3 network defined by larger A cations. We show that introduction of chemically mismatched octahedral cations into a cubic perovskite oxide parent phase modifies structure and composition beyond the unit cell length scale on the B sublattice alone. This affords an endotaxial nanocomposite of two cubic perovskite phases with distinct properties. These locally B-site cation-ordered and -disordered phases share a single AO_3 network and have enhanced stability against the formation of a competing hexagonal structure over the single-phase parent. Synergic integration of the distinct properties of these phases by the coherent interfaces of the composite produces solid oxide fuel cell cathode performance superior to that expected from the component phases in isolation.

■ INTRODUCTION

Assembly of separate phases within a single bulk grain is important in the production of structural and functional materials: it can determine the mechanical properties of steels[1] and optimize thermoelectric performance.[2] Vertical nanocomposites in heteroepitaxial thin films[3] enable combination of the properties of the component phases.[4] In the field of complex transition-metal oxides, chemical control and optimization of properties has conventionally relied on the modification of single-phase structures by targeted substitutions. This has had significant impact in areas as diverse as high-temperature superconductivity, batteries, solid oxide fuel cells, magnetism, ferroelectricity, and multiferroics. The structures adopted by complex oxides allow fine-tuning of physical behavior by chemical substitution, for example, the use of charge reservoir layers in superconducting copper oxides to remotely control the electron count in the electronically active CuO_2 planes.[5] The ABO_3 cubic perovskite $Ba_{0.5}Sr_{0.5}(Co_{0.8}Fe_{0.2})O_3$ has small d^n Co and Fe cations disordered on the B-sites of an AO_3 network defined by the larger Ba and Sr cations. It is a single-phase material because the similar charges and bonding chemistries of Co and Fe can be accommodated on a single site in the average structure, producing a combination of electronic (B-site d electrons) and oxide ion (anion vacancies) transport that makes it an effective solid oxide fuel cell (SOFC) cathode.[6] In this work, we explore the effect of incorporating the highly charged d^0 Mo^{6+} cation onto the B-site of this system. The distinct chemistry of this cation frustrates the formation of a single perovskite phase, as it does not match those of Co or Fe sufficiently to form single ordered or disordered distributions. We demonstrate the consequences of this charge frustration for the structure and properties. The system retains the perovskite structure by a structural and compositional phase separation, which occurs solely on the octahedral B-sites within a single AO_3 matrix. This AO_3 matrix is coherent throughout the micrometer-sized grains and templates the formation of two distinct perovskite phases. The dominant phase has no anion vacancies, but the endotaxial interfaces with the minority mixed ionic-electronic conductor (MIEC) phase give the nanocomposite unexpectedly good solid oxide fuel cell cathode performance.

■ EXPERIMENTAL SECTION

$Ba_{0.5}Sr_{0.5}Co_{0.8-x}Fe_{0.2-y}Mo_{x+y}O_{3-\delta}$ samples were initially prepared by solid-state synthesis. Stoichiometric amounts of the starting materials were mixed together by planetary ball milling (Fritsch Pulverisette 7) for 24 hours in 2-propanol with ZrO_2 balls, followed by drying, grinding, pressing into pellets, calcining at 700 °C for 6 hours, and finally heating to 900 °C for 8 hours. The resulting pellets were hand-

Received: April 11, 2013
Published: June 10, 2013

dx.doi.org/10.1021/ja403611s | *J. Am. Chem. Soc.* 2013, 135, 10114−10123

ground in an agate mortar and the powder was ball-milled further for 18 hours in 2-propanol. After being milled, the powder was dried, ground, pressed into pellets, and subsequently sintered in air at 1000 °C for 10 hours; the grinding/pellet pressing/heating step was repeated a total of four times to achieve phase purity and good homogeneity throughout.

Powder X-ray diffraction data were collected on a Panalytical X-pert Pro Bragg−Brentano geometry laboratory X-ray diffractometer. Synchrotron X-ray diffraction data were obtained on Beamline I11 at Diamond Light Source, U.K., and time-of-flight neutron diffraction (ND) data were collected on the high-resolution powder diffractometer (HRPD) instrument at the ISIS facility, Rutherford Appleton Laboratories. Structural parameters were refined by the Rietveld method, which is described in full in Supporting Information sections S3 and S4. The transmission electron microscopy (TEM) study was carried out on a JEOL JEM3010 (JEOL, LaB_6 filament, 300 keV), and energy-dispersive spectrometry (EDS) data were collected on a JEM2000FX (JEOL, W filament, 200 keV). High-angle annular dark field (HAADF) images were collected on a JEOL JEM 2100FCs, with a Schottky field emission gun operating in scanning tunneling electron microscopy (STEM) mode with a CEOS aberration-corrected probe. AC impedance measurements were recorded over the frequency range 1 MHz−0.01 Hz by use of a Solartron 1260 frequency response analyzer (FRA) with a modulation potential of 10 mV, over the temperature range 873−1073 K in static air. The symmetrical cell was held for 90 min at each temperature to allow thermal equilibration, and measurements were made with ZPlot v.2.9b (Scribner Associates) every 50 °C. The impedance arcs were modeled by use of equivalent circuit models (ECM) with ZView v.3.2b (Scribner Associates). All experimental procedures and analysis are described in detail in the Supporting Information.

■ RESULTS AND DISCUSSION

Phase Diagram Investigation. The perovskite structure of $Ba_{0.5}Sr_{0.5}(Co_{0.8}Fe_{0.2})O_{3-\delta}$ is shown in Figure 1a. Incorporation of Mo^{6+} on the B-site affords three distinct regions—correlated with low, intermediate, and high Mo contents—within the $Ba_{0.5}Sr_{0.5}(Co_{0.8-x}Fe_{0.2-y}Mo_{x+y})O_{3-\delta}$ phase field (Figure 2a) defined by X-ray diffraction (XRD) (details of the XRD analysis can be found in Supporting Information, section S3). We have chosen to highlight three compositions that are characteristic of low (**1**), intermediate (**2**), and high (**3**) Mo content.

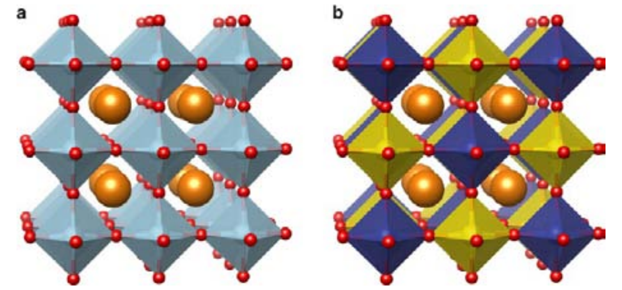

Figure 1. Crystal structures of (a) single perovskite (SP) and (b) double perovskite (DP). A-site cations are shown as orange spheres, and B-site cations are octahedrally coordinated by oxygen (red spheres) in the ABO_3 perovskite structure. The SP has a single B-site (shown in light blue) whereas the DP has an ordered arrangement of two different B-sites (shown in dark blue and yellow).

Low Mo contents [$x + y = z \leq 0.15$ for Co/Fe ratio $(0.8 - x)/(0.2 - y) = m \geq 4$; $z < 0.1$ for $m \leq 2$] afford a region with a single perovskite (SP) phase isostructural with $Ba_{0.5}Sr_{0.5}(Co_{0.8}Fe_{0.2})O_{3-\delta}$ (cell parameter $a_p \approx 3.8$ Å), with disordered substitution of Mo^{6+} onto the octahedral B-site

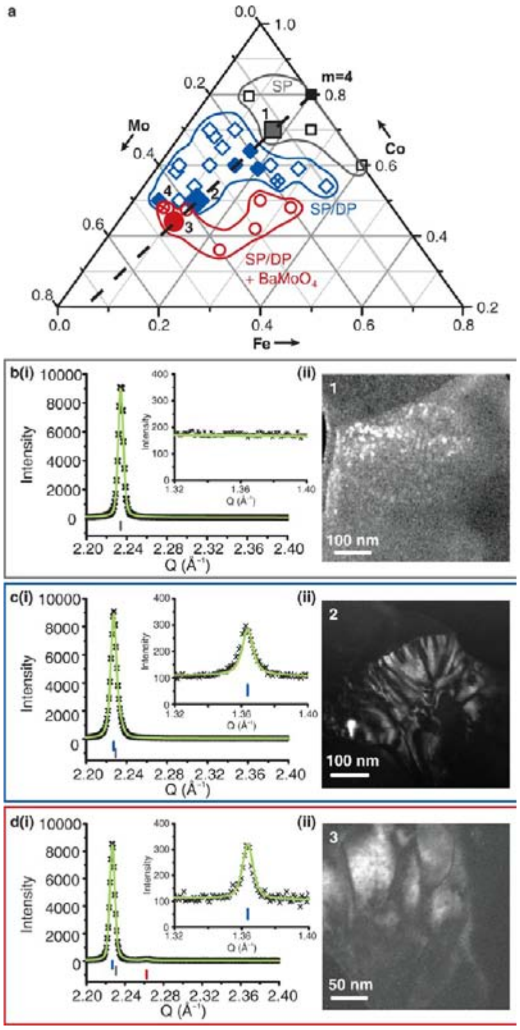

Figure 2. Overview of phase assemblage and microstructure. (a) B-site compositions studied in the $Ba_{0.5}Sr_{0.5}(Co_{0.8-x}Fe_{0.2-y}Mo_{x+y})O_{3-\delta}$ phase field classified according to the phase assemblage observed by XRD. The SP region is shown in gray, SP/DP in blue, and SP/DP/$BaMoO_4$ in red. The $m = 4$ black dashed line corresponds to a Co/Fe ratio of 4. Solid symbols indicate compositions for which the ASR was measured. The black square on the Co/Fe axis at $m = 4$ is the optimal composition for undoped (Ba,Sr)(Co,Fe) material (BSCF). Large symbols are compositions **1**, **2**, and **3** for which Rietveld refinements of XRD data and TEM images are shown in panels b, c, and d, respectively. The two points marked with crosses correspond to the SP and DP component phases refined for **2**. (i) Rietveld refinements of XRD data and (ii) DF TEM images of representative compositions in the three regions of the phase field are shown for (b) $z = 0.125$ (**1**, SP), (c) $z = 0.375$ (**2**, SP/DP), and (d) $z = 0.45$ (**3**, SP/DP + $BaMoO_4$) at $m = 4$. Reflection markers refer to SP (gray), DP (blue), and $BaMoO_4$ (red); the inset shows the region where the double perovskite superstructure reflection is observed, (a wider Q-space range for the inset is given in Supporting Information Figure S3, showing the major $BaMoO_4$ reflections). TEM was performed on [$1\bar{1}0$] oriented grains, with solely the [111]* superstructure reflections denoting the DP selected by the objective aperture. In the DF TEM images the darker regions are SP and the lighter regions are DP; in panel b (ii) for **1**, DP domains as shown here were observed in three out of 12 crystals, with average domain size 5−10 nm over a region that is approximately 100 × 200 nm^2; no DP reflections were detected by XRD. Supporting Information Figures S7 and S9 show that the microstructure of **2** persists throughout the SP/DP region of the phase diagram.

together with $Co^{2/3+}$ and $Fe^{3/4+}$ [$\delta \approx 0.5$ in $Ba_{0.5}Sr_{0.5}(Co_{0.8}Fe_{0.2})O_{3-\delta}$].[7] At the $m = 4$ Co/Fe ratio of the $Ba_{0.5}Sr_{0.5}(Co_{0.8}Fe_{0.2})O_{3-\delta}$ parent, the $z = 0.125$ material **1** adopts this SP structure (Figure 1a). At intermediate Mo content (into the region marked SP/DP on Figure 2a), a second perovskite phase coexists with the SP, with a doubled perovskite (DP) unit cell (Figure 1b, cell parameter $2a_p \approx 7.6$ Å) containing two distinct octahedral B-sites. This symmetry change is produced by cation ordering due to the size and charge differences between the first transition series d^n [0.645 Å high-spin (HS) Fe^{3+}, 0.745 Å HS Co^{2+}][8] and the second series d^0 Mo^{6+} (0.59 Å)[8] cations. This phase assemblage is adopted at $m = 4$ by the $z = 0.375$ composition **2** (Figure 2c). Further increase in Mo content results in the third region with the expulsion of $BaMoO_4$ (marked as SP/DP + $BaMoO_4$) coexisting with the SP/DP mixture, represented at $m = 4$ by the $z = 0.45$ composition **3** (Figure 2d).

Spatial Distribution and Orientational Relationship of SP and DP Phases. Dark-field (DF) imaging in the transmission electron microscope (TEM) shows DP coexists with SP on the nanometer scale within individual grains in the SP/DP region of the phase diagram [Figure 2c(ii)]. The microstructure is increasingly dominated by DP domains in the SP/DP + $BaMoO_4$ region [Figure 2d(ii)]. Selected area electron diffraction and DF images in the SP region [Figure 2b(ii)] reveal coexistence of pure SP grains with grains that are majority SP but contain 5−10 nm domains of the DP phase that are too small to be observed by XRD [Figure 2b(i)].

The locations, compositions, cation distributions, and atomic-scale structures of the DP and SP intragrain components in the SP/DP material $Ba_{0.5}Sr_{0.5}Co_{0.5}Fe_{0.125}Mo_{0.375}O_{3-\delta}$ (**2**) were evaluated by TEM (grain-specific, averaging over atomic columns and showing spatial relationships) and diffraction (bulk-sensitive XRD and neutron diffraction (ND), which both provide long-range volume-weighted information). The individual grains (Figure 3a) consist of an intergrowth of DP and SP phases with a range of domain sizes, some reaching the order of a hundred nanometers, while other areas have a complex arrangement of smaller domains of a few tens of nanometers in size (Figure 3b). Fourier transforms (FT) of separate areas of a high-resolution transmission electron microscopy (HRTEM) image of a single grain of **2** (Figure 3c) show (iii) distinct SP and (iv) B-site cation ordered DP domains oriented endotaxially (the FTs of the two domains have the same relationship to the grain). The image shows coherent interfaces between the SP and DP components with the cation positions lying on a single lattice.

Cation Distribution and Phase-Specific Crystal Chemistry. ND and XRD data (Figure 4) from **2** were refined simultaneously against a model of two discrete SP and DP phases (for full details see Supporting Information Section S4): this is an approximation, as it averages over the interphase boundary volume between the two components. The nominal cation composition of **2** was confirmed by EDS (Supporting Information Figure S2) and used to restrain the refinement, which produced a refined global B-site composition of $Co_{0.499(4)}Fe_{0.125(3)}Mo_{0.376(2)}$. As required by the endotaxial domain growth, the SP and DP have closely related a_p and $2a_p$ unit cell parameters with derived $a_p = 3.9861(2)$ and 3.9899(1) Å respectively, giving 0.095% mismatch strain. Mo^{6+} is accommodated in the composite by formation of the DP (70.4(1)%; Table 1 and Figure 5a), which is based on the Co^{2+}/Mo^{6+} charge-driven B-site alternation of $BaCo_{0.5}Mo_{0.5}O_3$.[9] The refined DP composition of $Ba_{0.5}Sr_{0.5}(Co_{0.483(3)}Fe_{0.018(2)})(Mo_{0.453(1)}Fe_{0.047(1)})O_{3.00(1)}$ is thus enriched in Mo over the global composition, with 96% and 90% occupancy of the two B-sites by Co and Mo, respectively.

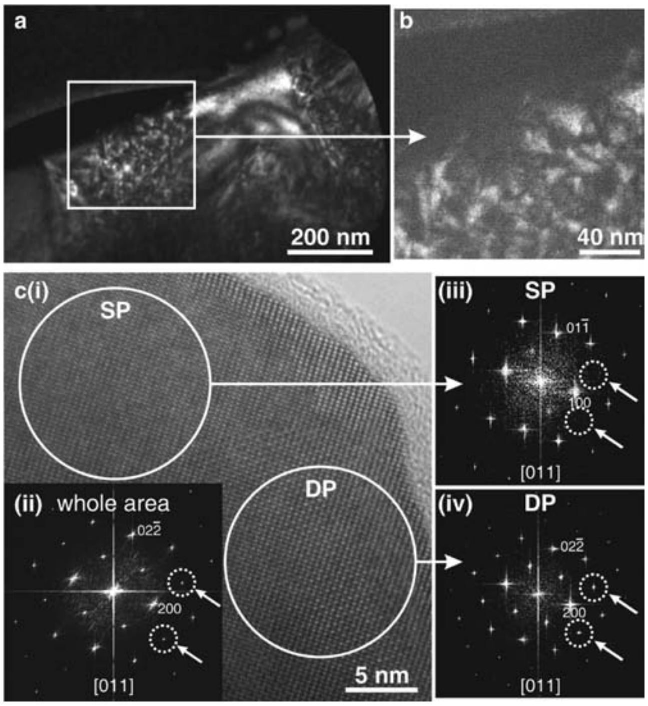

Figure 3. Intragrain phase separation in the $m = 4$ SP/DP material $Ba_{0.5}Sr_{0.5}Co_{0.5}Fe_{0.125}Mo_{0.375}O_{3-\delta}$ (**2**). (a) Dark-field image based on the double perovskite superstructure reflections, showing DP (light) and SP (dark) domains of a range of sizes within a single grain. (b) Higher magnification dark-field image showing an area where the SP and DP structures coexist on the nanometer scale. (c) (i) HRTEM image of a $[1\bar{1}0]$ oriented area and (ii) its Fourier-transformed (FT) diffraction pattern. The FT pattern is indexed as a double perovskite with the DP superstructure reflections indicated by white arrows. Simulation of the SP and DP regions from an HRTEM image of a single grain are shown in Supporting Information Figure S14. (iii) FT of a section (indicated by a white circle) of the area imaged in panel i. The FT diffraction pattern is indexed as a single perovskite (SP), with the absence of superstructure spots indicated by white arrows. (iv) FT of a second section of the same image (i), with the intense DP superstructure reflections emphasized by white arrows. The pattern is indexed as a double perovskite. The combination of images i, iii, and iv confirms the coexistence of single and double perovskite regions in individual crystallites of **2**.

Introduction of Fe^{3+} (oxidation state determined by Mössbauer spectroscopy; Supporting Information section S5 and Figure S12) into the 2+/6+ B-site array of the oxygen-stoichiometric DP respectively reduces and increases the charges of the Mo- and Co-based sublattices. In contrast to the Mo-rich character of this phase, Fe solubility in the DP is below that expected from the global composition, as it reduces the charge and composition imbalance between the B-sites and suppresses the cation order that defines this phase.

Fe-induced defects in the B-site ordering pattern are assimilated in the composite by the formation of the Fe-rich, Mo-deficient, B-site disordered SP phase $Ba_{0.5}Sr_{0.5}Co_{0.539(8)}Fe_{0.266(8)}Mo_{0.195(2)}O_{2.81(3)}$. This SP phase is isostructural with the parent material (Figure 5c) and, in contrast to the DP, contains anion vacancies. The refined O

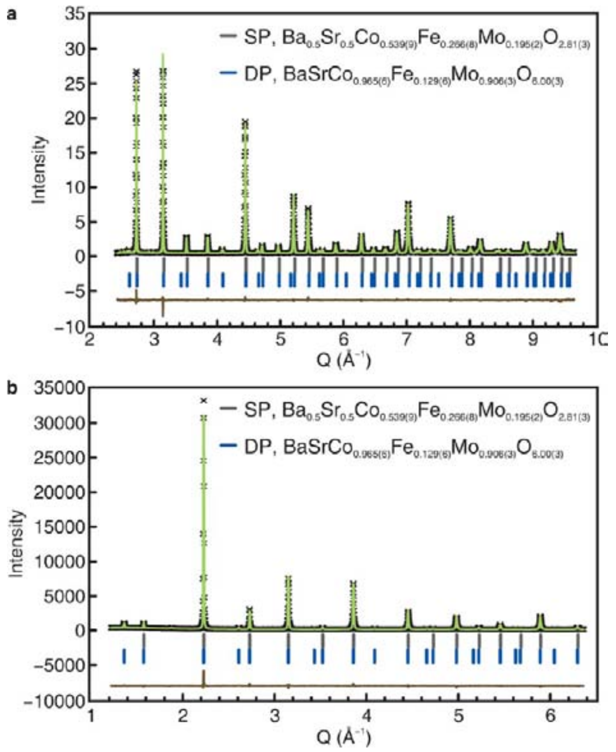

Figure 4. Final observed (black), calculated (green), and difference (brown) profiles from combined Rietveld refinement of powder diffraction data from (a) time-of-flight neutron diffraction (back-scattering bank) and (b) laboratory X-rays on $Ba_{0.5}Sr_{0.5}Co_{0.5}Fe_{0.125}Mo_{0.375}O_{3-\delta}$ (**2**) nominal composition. Tick marks show the Bragg reflections for SP in gray and DP in blue. Reliability factors for the two perovskite phase model are (a) R_{wp} 3.88%, R_{exp} = 2.80%, χ^2 = 1.92, R_{Bragg}(DP) = 1.97%, and R_{Bragg}(SP) = 1.52%; (b) R_{wp} = 6.96%, R_{exp} = 5.60%, χ^2 = 1.54, R_{Bragg}(DP) = 3.10%, and R_{Bragg}(SP) = 3.26%. Fits to all banks are shown in Supporting Information Figure S6. Refined oxygen content was verified by iodometric titration (Supporting Information section S6).

Table 1. Atomic Coordinates and Bond Lengths from Rietveld Refinement of Composition 2, $Ba_{0.5}Sr_{0.5}Co_{0.5}Fe_{0.125}Mo_{0.375}O_{3-\delta}$ (m = 4, z = 0.375)

Double Perovskite Phase				
$BaSrCo_{0.965(6)}Fe_{0.129(6)}Mo_{0.906(3)}O_{6.00(3)}$, a = 7.9798(3) Å				
weight fraction 0.7038(10), $Fm\bar{3}m$ (#225)				
atom	multiplicity	x, y, z	B_{iso} (Å^2)	occupancy
Ba	8c	0.25, 0.25, 0.25	0.62(3)	0.5
Sr	8c	0.25, 0.25, 0.25		0.5
Mo	4b	0.5, 0.5, 0.5	0.15(3)	0.906(2)
Fe1	4b	0.5, 0.5, 0.5		0.094(2)
Co	4a	0, 0, 0	0.22(9)	0.965(5)
Fe2	4a	0, 0, 0		0.036(5)
O	24e	0.2594(8), 0, 0	0.63(3)	1.000(4)
bond		n × distance (Å)	bond valence sums	
(Ba/Sr)−O		12 × 2.82211(3)	Ba/Sr 2.81/1.79	
(Mo/Fe1)−O		6 × 1.9272(7)	Mo/Fe1 5.68/3.81	
(Co/Fe2)−O		6 × 2.0628(7)	Co/Fe2 2.20/2.64	
Single Perovskite Phase				
$Ba_{0.5}Sr_{0.5}Co_{0.539(9)}Fe_{0.266(8)}Mo_{0.195(2)}O_{2.81(3)}$, a = 3.9861(2) Å				
weight fraction 0.2851(8), $Pm\bar{3}m$ (#221)				
atom	multiplicity	x, y, z	B_{iso} (Å^2)	occupancy
Ba	1a	0, 0, 0	0.41(6)	0.5
Sr	1a	0, 0, 0		0.5
Mo	1b	0.5, 0.5, 0.5	0.47(8)	0.195(2)
Fe	1b	0.5, 0.5, 0.5		0.266(8)
Co	1b	0.5, 0.5, 0.5		0.539(8)
O	3c	0.5, 0.5, 0	0.89(7)	0.938(10)
bond		n × distance (Å)	bond valence sums	
(Ba/Sr)−O		11.256 × 2.81863(3)	Ba/Sr 2.66/1.70	
(Co/Fe/Mo)−O		5.628 × 1.99307(3)	Co/Fe/Mo 2.49/2.99/4.46	

content and stability of Mo^{6+} in air allow the mean Co/Fe oxidation state in the SP to be calculated as +3, which with the Mössbauer determination of the Fe oxidation state as +3 gives an SP Co oxidation state of +3. The transition metal charges are Co^{3+} and Fe^{3+} in undoped $Ba_{0.5}Sr_{0.5}(Co_{0.8}Fe_{0.2})O_{3-\delta}$,[10] which has a much higher oxygen vacancy rate than the SP here. The reduced Mo content minimizes the occurrence of unfavorable Mo^{6+} near-neighbor pairs in the disordered SP. The global refined composition of **2** is $Ba_{0.5}Sr_{0.5}Co_{0.499(4)}Fe_{0.125(3)}Mo_{0.376(2)}O_{2.94(2)}$. Oxygen content was verified by iodometric titration as $O_{2.96(1)}$ (Supporting Information section S6), in agreement with the refined composition and consistent with a thermogravimetric analysis study (Supporting Information section S7). The overall O content of **2** is thus higher than the 2.75−2.4 range found for $Ba_{0.5}Sr_{0.5}(Co_{0.8}Fe_{0.2})O_{3-\delta}$.[7,10−12]

$Ba_{0.5}Sr_{0.5}Co_{0.499(4)}Fe_{0.125(3)}Mo_{0.376(2)}O_{2.94(2)}$ consists of a nanoscale assembly of 70.4(1)% $Ba_{0.5}Sr_{0.5}(Co_{0.483(3)}Fe_{0.018(2)})(Mo_{0.453(1)}Fe_{0.047(1)})O_{3.00(1)}$ (DP) and 29.6(1)% $Ba_{0.5}Sr_{0.5}Co_{0.539(8)}Fe_{0.266(8)}Mo_{0.195(2)}O_{2.81(3)}$ (SP). The observed SP/DP microstructure is persistent in the $Ba_{0.5}Sr_{0.5}(Co_{0.8-x}Fe_{0.2-y}Mo_{x+y})O_{3-\delta}$ materials because of the charge-based frustration of Mo-induced DP B-site order by Fe^{3+}, driving the intragrain compositional and structural segregation reflected in the refined compositions of the two component phases. Fe^{3+} substitution occurs preferentially on the Mo^{6+} site rather than the Co site in the DP for charge balance reasons. This produces low Fe solubility in the DP as high Fe contents will favor SP formation, thus explaining the persistence of the DP/SP single sublattice phase separation in all the materials investigated, while the common $AO_{3-\delta}$ network promotes intragrain coexistence, resulting in the associated microstructures. At the Mo content of **2**, the different chemistries of the three B-site cations thus drive the formation of two phases that are compositionally and structurally distinct but are endotaxially related. The DP is expected to be a pure electronic conductor whereas the oxygen vacancies in the SP make it a mixed ionic-electronic conductor (MIEC), demonstrating that distinct functions are generated by the phase separation.

The observed potential curves along the atomic columns in high-angle annular dark field (HAADF) images of different regions of a $[1\bar{1}0]$ oriented single grain of **2** agree with multislice simulations[13] based on the refined crystallographic models of each constituent phase within the composite (Figure 5b,d; details of the simulations are in Supporting Information section S8.1). The HAADF images show that the A sublattice is equivalent in DP and SP, whereas these regions differ in their B sublattice occupancy, in agreement with the diffraction work. The bulk diffraction methods further demonstrate the coherence of the $AO_{3-\delta}$ sublattice over which the B-site compositional and site-ordering cation separation occurs through the refined A-O distances of 2.81863(3) Å (SP) and

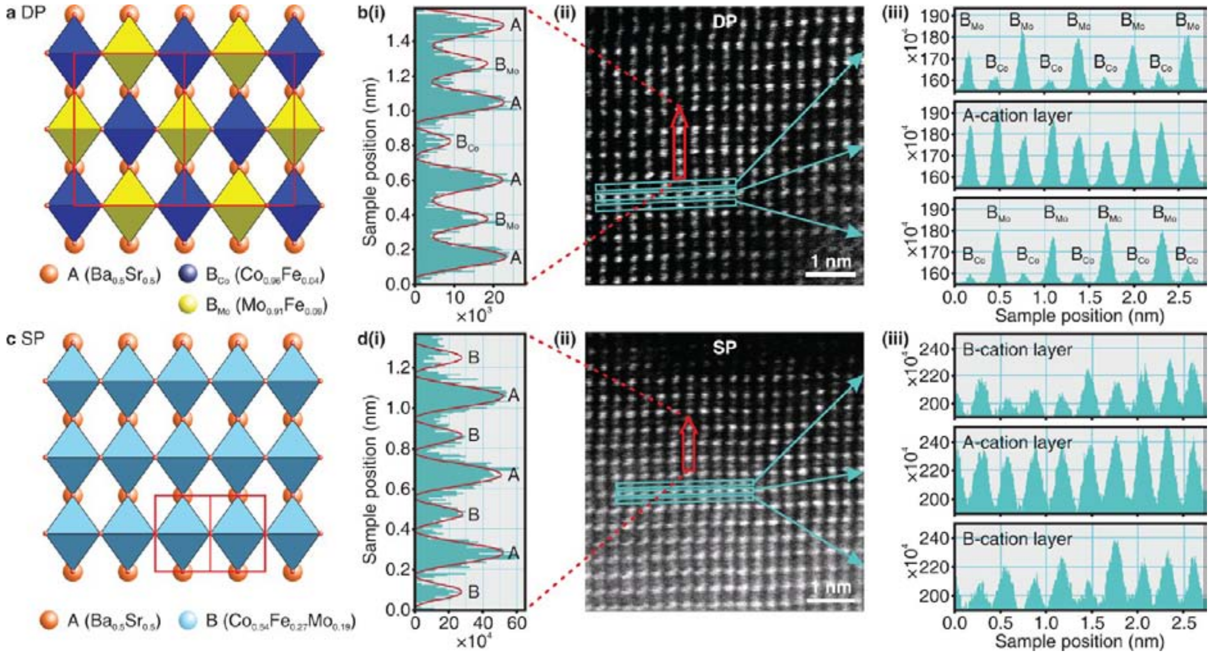

Figure 5. Chemical composition and cation ordering in component phases of the $m = 4$ SP/DP material $Ba_{0.5}Sr_{0.5}Co_{0.5}Fe_{0.125}Mo_{0.375}O_{3-\delta}$ (**2**). (a) Structure of the DP phase $Ba_{0.5}Sr_{0.5}(Co_{0.483(3)}Fe_{0.018(2)})_{0.5}(Mo_{0.453(1)}Fe_{0.047(1)})_{0.5}O_{3.00(1)}$ established from the combined refinements, viewed along the $[1\bar{1}0]$ direction, showing cation ordering on the octahedral B-sites, which produces separate columns of distinct composition [Mo-rich site (yellow) and Mo-poor site (dark blue)] in this orientation. The orientation shown is the same as that in the HAADF image [panel b (ii)]. (b) Intensity analysis of HAADF image (ii) for a $[1\bar{1}0]$ oriented DP region of a single grain. (i) QSTEM multislice simulation of a vertical line scan [indicated by the red arrow in (ii) and traversing A and B-sites, corresponding to the vertical direction in panel a] according to the refined composition of the DP phase. A- and B-sites are labeled showing the cation ordering; B_{Mo} and B_{Co} refer to the Mo-rich and Co-rich B-sites, respectively. The blue rectangles in (ii) indicate three lines of cations along which the variation of the intensity (corresponding to the horizontal direction in panel a) is shown in each case as indicated by the blue arrows to part (iii). Top and bottom rows correspond to B-sites (where the alternation between Co- and Mo-rich sites is clear), whereas the middle row corresponds to A-sites (homogeneous cation distribution). (c) SP phase $Ba_{0.5}Sr_{0.5}Co_{0.539(8)}Fe_{0.266(8)}Mo_{0.195(2)}O_{2.81(3)}$ established from the combined refinements, viewed along the same $[1\bar{1}0]$ direction. There is a single octahedral site. The orientation shown is the same as that in the HAADF image in panel d (ii). (d) Intensity analysis of HAADF image (ii) for a $[1\bar{1}0]$ oriented SP region of the same grain analyzed in panel b. (i) QSTEM multislice simulation of a vertical line scan [indicated by the red arrow in (ii), traversing A- and B-sites and corresponding to the vertical direction in panel c] according to the refined composition of the SP phase. A- and B-sites are labeled, showing the absence of B cation ordering in contrast to panel b (i). The absence of B-site order is shown in (iii) in the top and bottom line scans (corresponding to the horizontal direction in panel c) together with the homogeneous cation distribution in the middle A row.

2.82211(3) Å (DP). The DP O position is not fixed by symmetry, so the observed bond length match is not simply a consequence of the unit cell dimensions. There is thus a single $Ba_{0.5}Sr_{0.5}O_{3-\delta}$ network with constant, almost unstrained (0.12%) A–O distances spanning the coherent SP and DP phases defining each grain. The octahedral B-sites within this network are occupied in a spatially modulated manner by the three transition metal cations.

The separation into two structurally matched phases of distinct composition observed here is distinct from the order–disorder phenomena observed in materials such as relaxor ferroelectrics, which are compositionally homogeneous.[14] This is demonstrated by the observation of two distinct sets of cell parameters in the Mo-substituted materials studied here, which relaxes strain and leaves the different chemical bonding environments for the three cations achieved by the formation of two phases as the reason for the phase separation.

Thermal Stability of Phase-Separated and Single-Phase Materials. The effect of this nanoscale single sublattice phase separation on the stability of **2** was then investigated (full details in Supporting Information section S9). The stability after aging for 120 hours at 750 °C in air of $Ba_{0.5}Sr_{0.5}(Co_{0.8}Fe_{0.2})O_{3-\delta}$ and the Mo-substituted $Ba_{0.5}Sr_{0.5}(Co_{0.8-x}Fe_{0.2-y}Mo_{x+y})O_{3-\delta}$ phases at the constant Co/Fe ratio $m = 4$ is shown in Figure 6a (extended aging of **2** is shown in Figure 6b). The cubic perovskite structure is retained for the SP/DP composite **2**, whereas there is significant decomposition of the SP materials $Ba_{0.5}Sr_{0.5}(Co_{0.8}Fe_{0.2})O_{3-\delta}$ and $Ba_{0.5}Sr_{0.5}Co_{0.7}Fe_{0.175}Mo_{0.125}O_{3-\delta}$ (**1**) to a hexagonal perovskite. DC conductivity measurements in CO/CO_2 atmospheres (Supporting Information section S11) and X-ray analysis post-measurement (Figure 6b) reveal that **2** is stable to 10^{-10} atm O_2 and under 1600 ppm CO_2 at 700 °C; a reduction in lattice parameter was observed due to the loss of lattice oxygen, as observed for BSCF under similar conditions,[10] but no decomposition products were visible in the PXRD pattern. The SP/DP stabilization of the cubic structure extends to higher Co/Fe ratios (e.g., **4**, $m = 10$, $z = 0.45$). The B-site compositional and ordering segregation driven by Mo substitution in the SP/DP region of the phase field affords SP domains stabilized locally by enhanced Fe content over that of the global composition (higher Fe contents are known to stabilize pure cubic $Ba_{0.5}Sr_{0.5}(Co_{1-x}Fe_x)O_{3-\delta}$ against the formation of the hexagonal phase[15]) together with Co/Mo-rich DP stabilized by cation ordering and the absence of anion vacancies. Local compositions of the two component phases emerging from the B-site occupancy modulation within the coherent cubic $AO_{3-\delta}$ network defining the entire grain give the

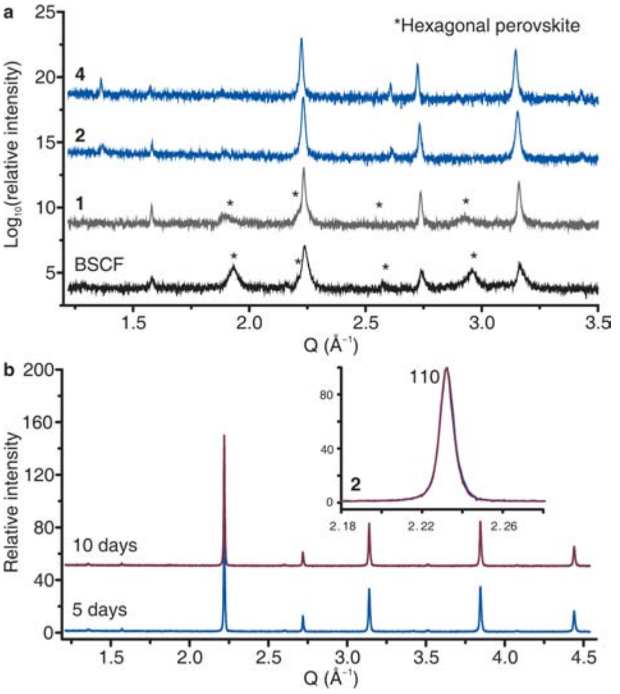

Figure 6. Thermal stability of perovskite structures in SP and SP/DP regions of the $Ba_{0.5}Sr_{0.5}(Co_{0.8-x}Fe_{0.2-y}Mo_{x+y})O_{3-\delta}$ system. (a) PXRD (logarithmic intensity scale) after aging at 750 °C for 120 h in air for $Ba_{0.5}Sr_{0.5}Co_{0.8}Fe_{0.2}O_{3-\delta}$ (BSCF, black, SP), $Ba_{0.5}Sr_{0.5}Co_{0.7}Fe_{0.175}Mo_{0.125}O_{3-\delta}$ **1** (gray, SP), $Ba_{0.5}Sr_{0.5}Co_{0.5}Fe_{0.125}Mo_{0.375}O_{3-\delta}$ **2** (blue, SP/DP), and $Ba_{0.5}Sr_{0.5}Co_{0.50}Fe_{0.05}Mo_{0.45}O_{3-\delta}$ **4** (blue, SP/DP). The appearance of hexagonal perovskite decomposition products is indicated by asterisks in the SP materials BSCF and **1**. (b) PXRD patterns (linear intensity scale) showing phase stability of **2** after long-term thermal aging: $Ba_{0.5}Sr_{0.5}Co_{0.5}Fe_{0.125}Mo_{0.375}O_{3-\delta}$ **2** was aged in air for 5 days (blue) and 10 days (purple) and aged in $pO_2 = 10^{-10}$ atm in the presence of ∼1600 ppm CO_2 (gray). No new phases were detected. (Inset) Superposition of the 10 days and 5 days PXRD patterns in the main figure over a narrower Q range, showing that the 110 cubic perovskite Bragg reflection common to the SP and DP phases is identical after aging in air.

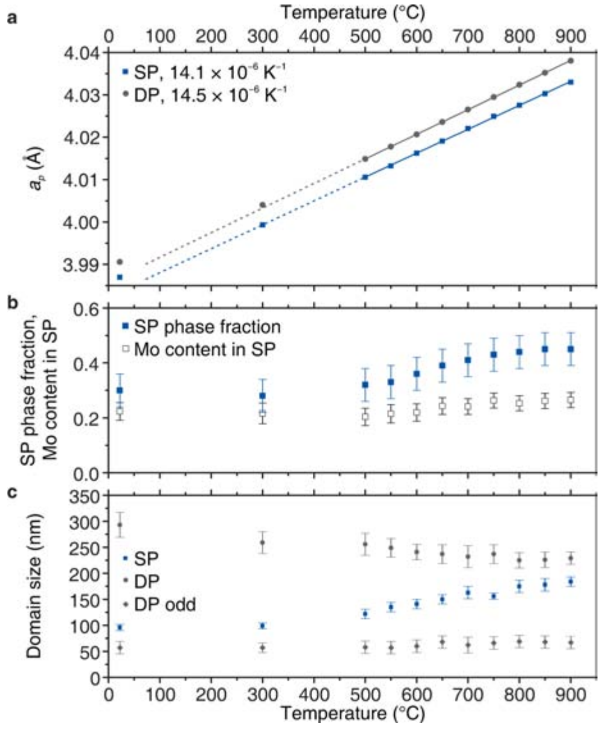

Figure 7. Microstructural and compositional features from Rietveld refinements of variable-temperature synchrotron X-ray diffraction data for **2**, $Ba_{0.5}Sr_{0.5}Co_{0.5}Fe_{0.125}Mo_{0.375}O_{3-\delta}$ ($m = 4$, $z = 0.375$). (a) Lattice parameter progression, expressed in terms of the single perovskite unit cell, a_p. Linear thermal expansion coefficients in the temperature range 500−900 °C (solid line) are given, and these are extrapolated to lower temperature to show a deviation from linearity (dashed line). (b) SP phase fraction and Mo content refined for the SP phase. (c) Volume-weighted domain sizes. DP odd refers solely to the supercell reflections for the DP, and as such represent the volume-weighted crystallite size of the DP in absence of any antiphase boundaries that may contribute to the DP subcell reflections. Error bars shown are 3 times the standard deviation from the refinements; in panel a, errors on the lattice parameters are on the fifth decimal place and therefore lie beneath the plotted symbols.

observed stability against the hexagonal perovskite. Charge frustration thus favors the cubic structure over the competing hexagonal perovskite structure.

Composition **2** was studied by powder X-ray thermodiffraction from 25 to 900 °C (Figure 7); above this temperature, it reacts with the quartz capillary. The prevalence of the domain structure was observed throughout this temperature range with little variation in phase fraction or Mo content of the SP phase (Figure 7b). Lattice parameters of the SP and DP phases increase linearly within a large part of the measured temperature range (Figure 7a). A deviation in linearity of the thermal expansion was found at lower temperatures, which can be attributed to a slight change in oxygen composition upon heating from room temperature to 500 °C, as has been observed previously for BSCF.[16] The lattice parameter difference between the phases remains nearly unaltered throughout the temperature range measured. This reflects the clamping of the lattice parameters due to the fixed $AO_{3-\delta}$ matrix within which the B-site compositional exchange takes place. This almost parallel evolution is characterized by linear thermal expansion coefficients from 500 °C that are very similar for the two phases (14.1×10^{-6} and 14.5×10^{-6} K^{-1} for SP and DP phases, respectively), while being smaller than values reported previously for BSCF in a similar temperature range (($19.0-22.9$) $\times$ 10^{-6} K^{-1}),[10,16] suggesting an improved compatibility with typical ceria-based electrolytes SDC ($Sm_{0.2}Ce_{0.8}O_{1.9}$, 11.4×10^{-6} K^{-1})[17] and GDC ($Gd_{0.2}Ce_{0.8}O_{1.9}$, 12.21×10^{-6} K^{-1})[18] when compared to BSCF. In parallel, the size of the SP and DP domains, as determined by analysis of sample broadening, showed little deviation within this temperature range (Figure 7c). Moreover, the biphasic character at the synthetic temperature was confirmed ex situ with a quenching experiment from 1000 °C, evidencing a mixture of 43(3)% SP and 57(3)% DP. The in situ experiment also showed a rearrangement of the domain structure from 500 to 800 °C that may be correlated with the oxygen loss detected by thermogravimetric analysis (TGA) occurring in this temperature range, provoking a different charge repartition in the $AO_{3-\delta}$ network as the average formal oxidation states of transition metals are reduced. Oxygen loss favors the expansion of oxygen-deficient SP domains, with a slight increase of their molybdenum content [from 0.20(2) to 0.25(2)], while DP domains are therefore contracted. Variation of the oxygen content is expected to have a dramatic effect on the domain structure as it is a compositional tool to influence the B-site chemical content in terms of electronic charges. The charge frustration maintains the observed phase separation over a wide temperature range, in contrast to the disappearance of this separation at the spinodal temperature seen, for example, in lead-based thermoelectric materials.

Electrochemical Properties. The $Ba_{0.5}Sr_{0.5}(Co_{0.8-x}Fe_{0.2-y}Mo_{x+y})O_{3-\delta}$ materials contain MIEC component phases and are potential SOFC electrodes. Symmetrical cells were prepared from selected compositions in the three regions of the phase field to evaluate their SOFC cathode performance by measurement of the area-specific resistance (ASR) (Figure 8a; Supporting Information section S10 and Table S11). The single-phase SP parent material $Ba_{0.5}Sr_{0.5}(Co_{0.8}Fe_{0.2})O_{3-\delta}$ itself is an MIEC and effective SOFC cathode that displays a range of ASR values from 0.03 to 10 $\Omega\cdot cm^2$ at 650 °C,[6,19] depending on processing conditions and electrolytes. The aim of this study is not to produce the lowest reported ASR for $Ba_{0.5}Sr_{0.5}(Co_{0.8}Fe_{0.2})O_{3-\delta}$-related cathodes but rather to examine the effect of charge frustration on structure and properties; here we measure an ASR of 0.15 $\Omega\cdot cm^2$ for the $Ba_{0.5}Sr_{0.5}(Co_{0.8}Fe_{0.2})O_{3-\delta}$ parent at 650 °C with $Ce_{0.8}Sm_{0.2}O_{2-\delta}$ electrolyte. Mo^{6+} is a component of heterogeneous catalyst systems involving dioxygen activation[20,21] and may enhance the oxygen reduction performance of the $Ba_{0.5}Sr_{0.5}(Co_{1-x}Fe_x)O_{3-\delta}$ family.

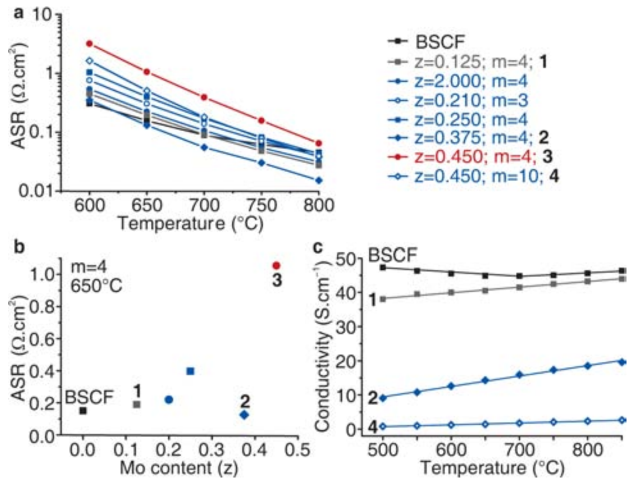

Figure 8. Physical properties and cathode performance in SP and SP/DP regions of the $Ba_{0.5}Sr_{0.5}(Co_{0.8-x}Fe_{0.2-y}Mo_{x+y})O_{3-\delta}$ system. (a) ASR of BSCFM compositions measured in air by AC impedance of symmetrical cells represented on a logarithmic scale between 600 and 800 °C. Colors are selected according to the location in the phase field shown in Figure 2a: black, BSCF; gray, SP; blue, SP/DP; red, SP/DP + $BaMoO_4$. $z = x + y$ is the Mo content; m is the Co/Fe ratio. (b) ASR at constant Co/Fe ratio ($m = 4$) with varying Mo content z at 650 °C, highlighting the anomalous nature of the $z = 0.375$ composition **2** (blue diamond). The same symbols are used for each composition as in panel a. (c) DC conductivity in air for the compositions given in panel a with the same color scheme. The conductivity decreases with increasing Mo content. The linear variation with temperature for **2** indicates that the changes in composition and microstructure on heating are minor, which is confirmed by Rietveld refinement of variable-temperature synchrotron X-ray diffraction data in Figure 7 and Supporting Information section S3.5 and by TGA data in Supporting Information section S7 and Figure S13.

ASR values measured for Mo-substituted materials range from 0.13 to 1.0 $\Omega\cdot cm^2$ at 650 °C. The lowest ASR is observed for $Ba_{0.5}Sr_{0.5}Co_{0.5}Fe_{0.125}Mo_{0.375}O_{3-\delta}$ (**2**), which is located in the SP/DP region ($z = 0.375$) and has the Co/Fe ratio $m = 4$ identified as optimal in the $Ba_{0.5}Sr_{0.5}(Co_{1-x}Fe_x)O_{3-\delta}$ family. The ASR of **2** is lower than that of $Ba_{0.5}Sr_{0.5}(Co_{0.8}Fe_{0.2})O_{3-\delta}$ between 650 and 800 °C (Figure 8a).

In order to separate compositional and porosity effects on electrode performance, we assessed the cathode microstructure by scanning electron microscopy (SEM) imaging and determined the surface area by gravimetric methods. Direct measurement of the pore volume by sorption measurements is challenging[22,23] due to the low masses of electrode material used relative to the dense SDC electrolyte used in the symmetrical cell configuration. We achieved this by using the identical screen-printing process for the cathode but onto thin Pt substrates supported on the electrolyte; once removed from the electrolyte support, this permitted gravimetric determination of N_2 sorption on the Pt-supported cathode and, once the cathode is dissolved by use of 3 M HCl, the Pt substrate itself (Figure 9a). The surface area of the cathode coating was calculated by point-by-point subtraction between data for the Pt-supported cathode and for the bare Pt foil [Figure 9b(ii)] to ensure that the observed weight difference could be solely ascribed to N_2 uptake for the cathode. The Brunauer–Emmett–Teller (BET) surface area was then calculated from the Pt-subtracted data by fitting the dependence of N_2 uptake with pressure to the BET equation[24] in the low pressure range [Figure 9b(iii)]. For full details of the subtractive technique, BET calculations, and BET surface area results for the tested cathodes, see Supporting Information section S10.4.

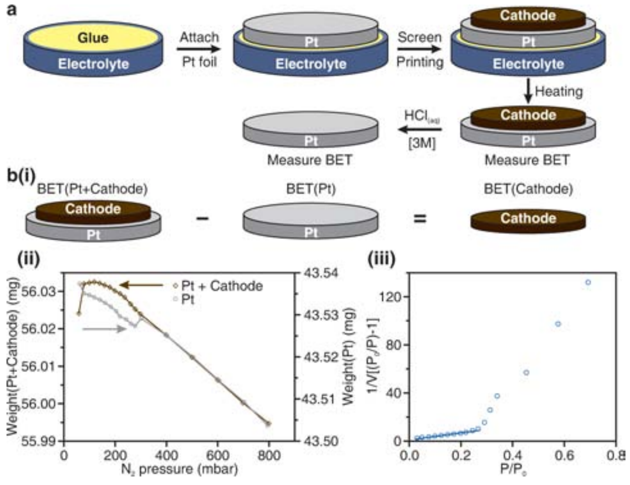

Figure 9. (a) Schematic of the preparation of Pt-supported cathode and subsequent acid removal of the cathode, as used for BET measurements. (b) (i) Scheme illustrating the subtractive protocol used to calculate the surface area of the cathodes. (ii) Observed weight gain with N_2 pressure for a cathode sample of **2** prepared by the method outlined in panel a and for the bare Pt substrate. (iii) BET fitting (blue line) for the low-pressure region of N_2 sorption data (blue circles) obtained from the difference between as-made Pt supported cathode, **2**, and bare Pt substrate.

This subtractive technique allowed direct determination of the electrode pore volume across the series (Table 2), giving a trend in agreement with the SEM observations (Supporting Information section S10.4 and Figure S17); similar surface areas were observed for all the Mo-substituted systems, which were systematically larger than those found for the $Ba_{0.5}Sr_{0.5}(Co_{0.8}Fe_{0.2})O_{3-\delta}$ parent under the processing con-

Table 2. BET Parameters and Derived Surface Areas of the Printed Cathodes from the Point-by-Point Subtractive Technique[a]

sample	C	V_m (mmol·g^{-1})	BET (m^2·g^{-1})
BSCF	996.0	$7.200 \times 10^{-3} \pm 5.770 \times 10^{-4}$	0.70 ± 0.06
1	18.5	$3.270 \times 10^{-2} \pm 7.730 \times 10^{-4}$	3.19 ± 0.08
2	23.9	$3.261 \times 10^{-2} \pm 1.870 \times 10^{-4}$	3.18 ± 0.02
4	37.7	$3.098 \times 10^{-2} \pm 6.790 \times 10^{-4}$	3.02 ± 0.07

[a] C is the BET constant and V_m is the monolayer adsorbed gas quantity.

ditions used. Direct ASR comparisons are thus valid within the Mo-substituted series.

Evolution of the ASR with increasing Mo content z at the Co/Fe ratio $m = 4$ is nonmonotonic (Figure 8b), although the total DC conductivity σ_{DC} (Figure 8c and Supporting Information section S11) decreases as expected from the reduction in d electron and oxygen vacancy concentration on substitution of d^n by d^0 Mo^{6+} cations. This suggests that Mo catalyzes the oxygen reduction reaction (ORR), consistent with its role in catalytic systems involving dioxygen activation. The ASR of **2** ($z = 0.375$) is lower than that of both SP [$z = 0.125$ (**1**)] and SP/DP ($z = 0.2$, 0.25) materials with reduced Mo contents. It is also lower than that of both $z = 0.45$ (**3**) from the SP/DP/BaMoO$_4$ region and lower Fe content $m = 10$, $z = 0.45$ (**4**) in the SP/DP region. AC impedance arcs at 650 °C [Figure 10a(i)] show that both SP/DP **2** and SP $Ba_{0.5}Sr_{0.5}(Co_{0.8}Fe_{0.2})O_{3-\delta}$ display similar impedance responses dominated by a Gerischer-type contribution [Figure 10a(ii)], which is colimited by oxygen surface exchange and bulk oxide transport.[25] All the other higher ASR $Ba_{0.5}Sr_{0.5}(Co_{0.8-x}Fe_{0.2-y}Mo_{x+y})O_{3-\delta}$ materials display different responses associated with charge transfer (electronic) and mass transport (chemical) processes (detailed discussion can be found in Supporting Information sections S10.6–S10.9). These comparisons suggest the superiority of the SP/DP architecture of **2** over the SP-only **1** (despite a lower DC resistance for **1**), together with the improved performance of this architecture at **2** in comparison with, for example, **4** ($m = 10$, $z = 0.45$). The relationship between Mo content (and related factors such as oxygen nonstoichiometry, SP phase fraction, and σ_{DC}) and ASR implicates the observed SP/DP intragrain microstructure in the cathode performance. The mechanistic similarity between **2** and $Ba_{0.5}Sr_{0.5}(Co_{0.8}Fe_{0.2})O_{3-\delta}$ demonstrated by the impedance responses suggest that this SP/DP assembly can give cathode performance comparable to best-in-class single-phase materials, despite being compositionally dominated by an ionic insulator. The self-organization of the endotaxial composite confers higher stability than the single-phase parent and opens up the possibility of further optimization in this family of SOFC cathode materials.

The microstructure of **2** can be approximated as a coherent endotaxial intergrowth of a pure electronic conductor (DP, with no oxygen vacancy content but noninteger transition-metal valence: active in the ORR in isolation only at the triple phase boundary with electrolyte and air) and a MIEC (SP, with vacancies for oxide transport and ORR active at all interfaces with air) (Figure 10b). The pathways for electronic conduction are throughout and between the DP and SP regions, whereas oxide ion transport is restricted to the interconnected SP phase regions and their surfaces, including interfaces with the DP. The microstructure of Figure 10b creates a high-surface-area triple phase boundary for O^{2-} formation where the electronically conducting, catalytically active DP meets the MIEC SP and air, with the single AO$_{3-\delta}$ network interfaces between SP and DP assisting oxide transfer between them. The SP

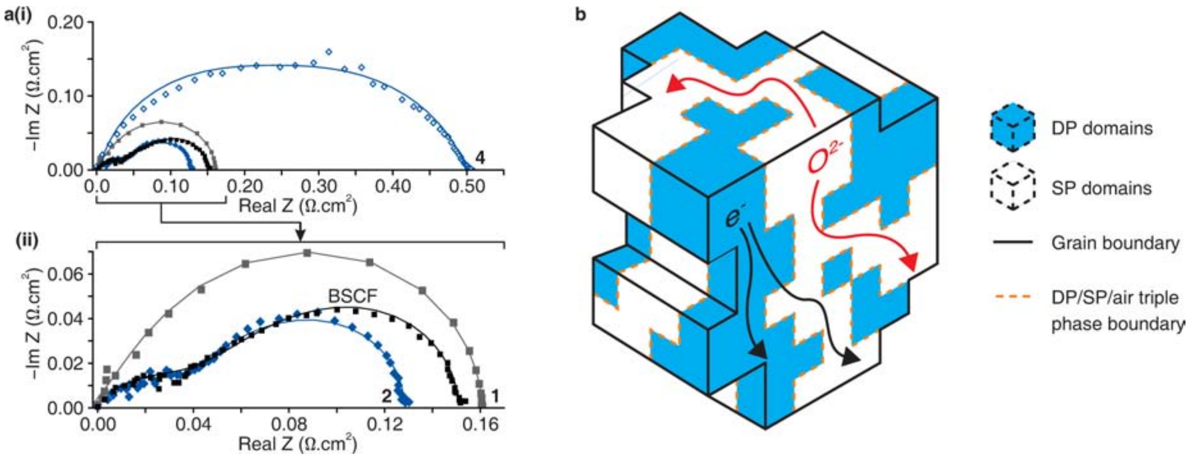

Figure 10. (a) (i) Electrochemical impedance spectroscopy (EIS) arcs for the compositions given in Figure 8a (with the same color scheme) at 650 °C (arcs have been normalized to 0 on the x-axis to remove the electrolyte contribution): symbols are measured data, and lines are from fitting of equivalent circuit models (ECM; Supporting Information section S10.6 and Figure S19). The same electrode processes are identified from the ECM for **2** and BSCF, and differ from those occurring in **1** and **4**. Composition **4** ($m = 10$) is shown here, as it has lower ASR than **3** ($m = 4$), which is shown in Supporting Information Figure S19d. (ii) Close-up of the EIS arcs for **1**, **2**, and BSCF shown in panel i. As each cathode was manufactured by the same protocol (milling regime, ink processing, screen printing parameters, and thermal treatment) and displays similar morphology and surface area (Supporting Information section S10.4), differences in the observed arcs and selected ECM are a reflection of differences in the electrochemical properties of each composition. HRTEM and XRD studies show the phase assemblage and microstructure were unaffected by preparation of the symmetrical cells (Supporting Information section S10.2 and Figure S15). The Gerischer-type half-tear-drop shape is apparent in the AC impedance arcs of **2** and BSCF as the dominant large-resistance arc. (b) Schematic representation of oxygen ion (red) and electron (black) transport pathways available in a two-phase endotaxial composite grain of **2**. The absence of oxygen vacancies makes the DP (blue) a pure electronic conductor, whereas oxygen mobility is possible within the SP and along the SP/DP interfaces. The SP/DP/air triple phase boundary of **2** is highlighted as an orange dotted line; this boundary, as well as the surface of the SP MIEC regions, is active in the ORR.

component of **2** is richer in Fe than the global $m = 4$ composition, and thus expected to be a poorer cathode than $m = 4$ $Ba_{0.5}Sr_{0.5}(Co_{0.8}Fe_{0.2})O_{3-\delta}$, on the basis of variation of $Ba_{0.5}Sr_{0.5}(Co_{1-x}Fe_{x})O_{3-\delta}$ performance with Fe content.[26] The presence of 70 wt % DP in **2** would be expected to lead to poor cathode performance due to reduced electronic conductivity and absence of oxygen vacancies. This is not the case, however: 30 wt % SP alone is not sufficient to account for the low ASR value of **2**, as SP/DP $Ba_{0.5}Sr_{0.5}(Co_{0.8-x}Fe_{0.2-y}Mo_{x+y})O_{3-\delta}$ materials such as $m = 3$, $z = 0.21$ [63(2)% SP] with higher SP content have higher ASR (Figure 8a,b). This shows that the DP is not a spectator phase and that its high Mo and Co content contributes to the oxygen reduction performance of the nanocomposite **2**, whose structure favors synergic interaction of the DP and the oxide ion-conducting SP. The functional behavior of **2** suggests that the coherent $AO_{3-\delta}$ network can integrate the properties of the distinct SP and DP regions to produce performance from the composite that is superior to that expected from the local component phases in isolation.

■ CONCLUSION

Composition **2** has superior cathode performance to the other SP/DP materials evaluated because its interplay of SP/DP ratio, domain sizes, phase compositions, and spatial locations best combines the distinct properties of SP and DP. It is stabilized by local separation into compositionally and structurally distinct domains of Fe-rich SP and cation-ordered, anion vacancy-free Mo-rich DP, which are spanned by a single $AO_{3-\delta}$ network. This microstructure results from a heterogeneous distribution of the three electronically active cations over the B-sites. The perovskite structure adapts to the compositional complexity and contraindicated chemistry of the three B-site cations that frustrate the formation of a single phase by this reorganization correlated beyond the unit cell. The resulting nanoscale modulation of the B-site occupancy produces the compositionally and structurally distinct endotaxially related phases forming the composite. The matching of cation occupancy to the crystal chemical environment that is possible in the two-phase B-site separation within a single $AO_{3-\delta}$ network increases the stability of the cubic perovskite with respect to competing structures over that of the single-phase parent material. The SP/DP composite performs well as an SOFC cathode, exceeding expectations based on the local compositions of the constituent phases (one of which is not capable of anion transport). The stability of the self-organized endotaxial composite is thus determined by the local phase compositions, but its properties surpass the sum of these local components in isolation because of the synergic integration of the functions of the two phases by the coherent interfaces of the composite. The chemical frustration produced by charge and bonding differences drives the self-assembly of compositionally and structurally ordered regions, spanned by a common network. This frustration-based approach is clearly well-suited to the diverse cation ordering patterns known in perovskites.[27] The single sublattice phase separation and resulting property integration may also prove applicable to the many well-known families of complex oxides that feature separate structural networks.

■ ASSOCIATED CONTENT

Ⓢ Supporting Information

Additional text, 11 tables, and 22 figures with information on synthesis methods, analysis of powder diffraction data, Mössbauer spectroscopy, iodometric titration, thermogravimetric analysis, transmission electron microscopy, thermal stability, and electrochemical testing. This material is available free of charge via the Internet at http://pubs.acs.org.

■ AUTHOR INFORMATION

Corresponding Author

m.j.rosseinsky@liv.ac.uk; claridge@liv.ac.uk

Author Contributions

⊥A.D., R.S., and M.A.T. contributed equally.

Notes

The authors declare no competing financial interest.

■ ACKNOWLEDGMENTS

This work was carried out with the support of the European Research Council (ERC Grant agreement 227987 RLUCIM), EPSRC (EP/H000925), and STFC [Diamond Light Source (DLS) and ISIS (Rutherford Appleton Laboratory)]. M.J.R. is a Royal Society Research Professor. We thank Chiu Tang, Julia Parker, and Stephen Thompson for assistance in using beamline I11 (DLS) and Aziz Daoud-Aladine for assistance in using HRPD (ISIS). We thank EPSRC for a studentship for M.A.T.

■ REFERENCES

(1) Tsuji, N.; Ueji, R.; Minamino, Y.; Saito, Y. *Scr. Mater.* **2002**, *46*, 305−310.

(2) Hsu, K. F.; Loo, S.; Guo, F.; Chen, W.; Dyck, J. S.; Uher, C.; Hogan, T.; Polychroniadis, E. K.; Kanatzidis, M. G. *Science* **2004**, *303*, 818−821.

(3) MacManus-Driscoll, J. L. *Adv. Funct. Mater.* **2010**, *20*, 2035−2045.

(4) Zheng, H.; Wang, J.; Lofland, S. E.; Ma, Z.; Mohaddes-Ardabili, L.; Zhao, T.; Salamanca-Riba, L.; Shinde, S. R.; Ogale, S. B.; Bai, F.; Viehland, D.; Jia, Y.; Schlom, D. G.; Wuttig, M.; Roytburd, A.; Ramesh, R. *Science* **2004**, *303*, 661−663.

(5) Cava, R. J. *J. Am. Ceram. Soc.* **2000**, *83*, 5−28.

(6) Shao, Z.; Haile, S. M. *Nature* **2004**, *431*, 170−173.

(7) Vente, J.; McIntosh, S.; Haije, W.; Bouwmeester, H. *J. Solid State Electr.* **2006**, *10*, 581−588.

(8) Shannon, R. *Acta Crystallogr. A* **1976**, *32*, 751−767.

(9) Martinez-Lope, M. J.; Alonso, J. A.; Casais, M. T.; Fernandez-Diaz, M. T. *Eur. J. Inorg. Chem.* **2002**, 2463−2469.

(10) McIntosh, S.; Vente, J. F.; Haije, W. G.; Blank, D. H. A.; Bouwmeester, H. J. M. *Chem. Mater.* **2006**, *18*, 2187−2193.

(11) McIntosh, S.; Vente, J. F.; Haije, W. G.; Blank, D. H. A.; Bouwmeester, H. J. M. *Solid State Ionics* **2006**, *177* (19−25), 1737−1742.

(12) Jung, J. -I.; Misture, S. T.; Edwards, D. D. *Solid State Ionics* **2010**, *181* (27−28), 1287−1293.

(13) Koch, C. T. Determination of core structure periodicity and point defect density along dislocations. Ph.D. Thesis, Arizona State University, 2002.

(14) Cross, L. E. *Ferroelectrics* **1987**, *76* (3−4), 241−267.

(15) Jung, J.-I.; Edwards, D. *J. Mater. Sci.* **2012**, *46* (23), 7415−7422.

(16) Zhu, Q.; Jin, T.; Wang, Y. *Solid State Ionics* **2006**, *177*, 1199−1204.

(17) Sameshima, S.; Ichikawa, T.; Kawaminami, M.; Hirata, Y. *Mater. Chem. Phys.* **1999**, *61*, 31−35.

(18) Prashanth Kumar, V.; Reddy, Y. S.; Kistaiah, P.; Prasad, G.; Vishnuvardhan Reddy, C. *Mater. Chem. Phys.* **2008**, *112*, 711−718.

(19) Lim, Y. H.; Lee, J.; Yoon, J. S.; Kim, C. E.; Hwang, H. J. *J. Power Sources* **2007**, *171*, 79−85.

(20) Cavani, F.; Centi, G.; Marion, P. Catalytic ammoxidation of hydrocarbons on mixed oxides. In *Metal Oxide Catalysis*; Jackson, S.

D., Hargreaves, J. S. J., Eds.; Wiley−VCH Verlag: Weinheim, Germany, 2009.

(21) Deng, Z. Q.; Smit, J. P.; Niu, H. J.; Evans, G.; Li, M. R.; Xu, Z. L.; Claridge, J. B.; Rosseinsky, M. J. *Chem. Mater.* **2009**, *21*, 5154−5162.

(22) Fleig, J. *Annu. Rev. Mater. Res.* **2003**, *33*, 361−382.

(23) Vohs, J. M.; Gorte, R. J. *Adv. Mater.* **2009**, *21*, 943−956.

(24) Brunauer, S.; Emmett, P. H.; Teller, E. *J. Am. Chem. Soc.* **1938**, *60*, 309−319.

(25) Adler, S. B.; Lane, J. A.; Steele, B. C. H. *J. Electrochem. Soc.* **1996**, *143*, 3554−3564.

(26) Chen, Z.; Ran, R.; Zhou, W.; Shao, Z.; Liu, S. *Electrochim. Acta* **2007**, *52*, 7343−7351.

(27) Davies, P. K.; Wu, H.; Borisevich, A. Y.; Molodetsky, I. E.; Farber, L. *Annu. Rev. Mater. Res.* **2008**, *38*, 369−401.